arXiv:1704.02633v1 [cond-mat.soft] 9 Apr 2017

Self-Organization of Self-Clearing Beating Patterns in an Array of Locally Interacting Ciliated Cells Formulated as an Adaptive Boolean Network

Martin Schneiter, Jaroslav Rička, and Martin Frenz*
Institute of Applied Physics, University of Bern, Sidlerstrasse 5, 3012 Bern, Switzerland
(Dated: April 11, 2017)

The observed spatio-temporal ciliary beat patterns on multiciliated epithelia are suspected to be the result of self-organizing processes on various levels. Here, we present an abstract epithelium model at the pluricellular level, which intends to make the self-organization of ciliary beating patterns as well as of the associated fluid transport across the airway epithelium plausible.
Ciliated cells are modeled in terms of locally interacting oscillating two-state actuators. The local interactions among these boolean actuators are triggered by seeded mucus lumps. In the course of a simulation the actuators' state and the associated mucus velocity field self-organize in tandem.
We suggest to consider the dynamics on multiciliated epithelia in the context of adaptive (boolean) networks. Within the framework of adaptive boolean networks ciliated cells represent the nodes and as the mucus establishes the local interactions among nodes, its distribution determines the topology of the network.
Furthermore, we present the results and insights from comprehensive parameter studies. The results show evidence that so called deterministic update schemes, which are meant to represent intercellular signaling, lead to more realistic and robust dynamics and may therefore be favored by nature.
Finally, we suppose that unciliated cells introduce a modular network topology on ciliated epithelia causing the self-organization taking place simultaneously in each "ciliated module". This reasoning provides the first consistent explanation for the meaning of the observed patchy expression patterns of the mucus modulation wave fields. Modularity may therefore be seen as a modular construction plan of nature for ciliated epithelia whose number of cells range over several order of magnitudes.

I. INTRODUCTION

Motivation for the present work is to contribute to the understanding of the fascinating and omnipresent phenomenon of mucociliary transport.

The epithelium of our airways constitutes a self-cleaning surface protecting our lungs from a variety of inhaled particles such as exhaust, dust, bacteria and other harmful substances of micro- and submicrometer size. These particles get entrapped by the mucus layer lining the inner surface of the tracheal and pulmonary airways, which is propelled by the coordinated oscillatory movement of millions of subjacent cilia. Cilia are hair-like protrusions of the cell membrane, an overview of their structure and function can be found in [1, 2].

To gain insight into the mucociliary clearing mechanism, many experimental techniques on various length- and time-scales are conducted. Experimental studies typically focus either on a structural or functional component on a typical scale, like the remarkable insight into the detailed molecular structure of the axoneme (see e.g. [3, 4]), the orientation of the ciliary beating plane [2], the distribution of the different epithelial cell types (e.g. [5, 6]) or the observation of mucociliary phenomena on the pluricellular level [7]. Even though much work has been done on various scales, our understanding of the basic mesoscopic function of the system still appears rather limited. Experimental methods face several challenges: until today, it is not possible to observe the details of the mucociliary dynamics in vivo. Further, it is difficult to observe the mucociliary clearing mechanism under controlled conditions. And finally, it is highly complex and laborious to simultaneously measure structural and functional parameters at different scales.

Mathematical models are perfectly suited to conduct parameter studies in order to determine the effects of structural and functional parameters on mucociliary phenomena and therefore, serve as an alternative approach for the investigation of the intriguing mucociliary phenomena. Based on the qualitative observations and interpretations, numerous mathematical models have been developed and the development still continues, as the surge of computing power allows to treat models of increasing complexity. Considering the implementation of mucociliary interactions the existing models can roughly be divided into two classes.
One class of models prescribes the motion of cilia, including their coordination, and concentrates on the hydrodynamics and rheology of the system. In these models the action of cilia is modeled as distributed oscillating momentum source, such as oscillating envelope [8], traction layer [9], active porous medium or oscillating array of cilia represented by a distribution of hydrodynamic singularities along the cilia's centerline [10]. The aim of these studies is to elaborate the geometrical and rheological conditions under which the system achieves an efficient transport (e.g. [11]).
More relevant to the context of the present study is a

* martin.frenz@iap.unibe.ch

second class of models, aimed at the understanding of the emergence of the pattern of motion. In these models the details of the motion of cilia or their coordination are not prescribed explicitly. The coordinated behavior rather emerges in the course of self-organization, during which the system components interact locally, what drives the system from an initially uncoordinated state towards a globally coordinated state exhibiting cooperative behavior.
Self-organization may play a role on various time- and length-scales, at various levels for the generation of mucociliary transport. As discussed in [12] the interactions between cilia-generated fluid flow and planar cell polarity (PCP) signaling may lead to self-organization during the morphogenesis, which establishes the alignment of the axonemes on the individual cells. Much of work has been done on the molecular level, concerning the molecular motors (dynein motor proteins), their organization in the axoneme as well as the hydrodynamics of the resulting model cilium (eg. [13–15]). The complex motion pattern of a single cilium is thought to result from the self-organization of many dynein motor proteins generating stresses on the elastic microtubules in the axoneme. The next higher level, the cellular level, concerns the formation of metachronal waves by the self-organized synchronization of cilia covering a single cell [16]. For a long time it remained an open question whether the synchronization is achieved by cellular signaling (membrane potentials and calcium waves), or if it emerges spontaneously, due to interactions between the individual cilia. Today, the computational models indicate that hydrodynamic coupling is sufficient to induce synchronization [16–18]. It is conceivable, however, that calcium signaling is needed for fine tuning the synchronization [19].

Here we propose a first step to the next higher level, the pluricellular level, on which the self-organization of ciliary activity among ciliated cells is thought to generate the global wave field and fluid transport on the airway epithelium. In order to make the self-organized beat patterns as well as self-organized fluid transport across the airway epithelium plausible, we present an oversimplified model, which is intended to represent a virtual self-cleaning epithelium. Ciliated cells are modeled as actuators alternating between two possible states representing ciliary oscillations. Interactions between the two-state actuators are mediated by discrete mucus lumps and enmeshed dust particles. Whenever it is possible, the mucus droplets get displaced by the action of actuators and they may block their motion in certain configurations, which is prescribed by local interaction rules. This highly simplified model based on locally interacting motors self-organizes towards a virtual self-cleaning epithelium: the initially randomly distributed phases erratically displace the mucus lumps at the beginning of the simulation. As time passes the motors self-organize, which is expressed by emergent global spatio-temporal structures, resembling the metachronal wavelets, which have been observed on the ciliated tracheal epithelium [7]. These metachronal wavelets efficiently transport the mucus lumps into a well defined direction.

This paper is organized as follows. In Sec. II we introduce our abstract epithelium model based on symmetrically interacting two-state actuators. The local mucociliary interactions are first formulated in an intuitive way, before they are reformulated as logical update functions of the local state and mucus distribution. The goal of Sec. II is to formulate our epithelium model in terms of an adaptive boolean network. Within the framework of adaptive boolean networks nodes are represented by actuators. The topology of the network (in effect the links between the nodes) is determined by the mucus distribution. Furthermore, we introduce the involved model parameters encompassing in particular different morphologies, boundary conditions and update schemes. Thanks to the simplicity of our epithelium model, it is possible to investigate the impact of these model parameters on the system dynamics by conducting comprehensive parameter studies. The corresponding simulation data are presented in Sec. III. The simulation data have been screened for any suspicious coherences between model parameters and network dynamics. Furthermore, we aimed at finding the mechanisms driving the model efficiently towards properly self-cleaning states. Finally, in Sec. IV we discuss our findings and their meaning for the real biological system.

II. MODEL DESCRIPTION

A. Symmetrically Interacting Two-State Actuators

Our model is based on symmetrically interacting two-state actuators. Each actuator represents a ciliated epithelial cell. By arranging many actuators in a parquet-like manner, the model represents a ciliated epithelium. Cilia corresponding to the same cell are assumed to move synchronously back and forth. This back and forth motion of cilia bundles is incorporated by the alternation between the actuators' two possible states, which is illustrated in Fig.1. The actual state of an actuator can thus be expressed by the boolean state variable $\psi \in \{0, 1\}$.

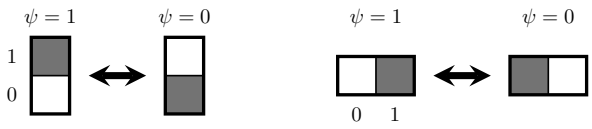

FIG. 1. Ciliated cells are represented by two-state actuators. An actuator's current state is expressed by the boolean state variable ψ. Each actuator provides two fields (0 and 1).

B. Morphology of Virtual Epithelia

The morphology of the airway epithelium is thought to be the result of self-organizing processes during the morphogenesis [12]. An important characteristic of the morphology is the distribution of the orientation of the ciliary beating plane, which can be determined by the orientation of the microtubules in the axoneme [2]. The impact of the (dis-)orientation of the ciliary beating plane i.e. of the axonemal orientation on mucociliary transport has been discussed e.g. in [20, 21]. It has been concluded that a disorganized ciliary orientation may be a primary cause for mucociliary dysfunction and vice versa. Studies attempting to quantify the axonemal orientation of respiratory cilia usually determine the ciliary beating plane on a few cells derived from nasal brushing (e.g. [22]). To the best of our knowledge, possible differences between the intra- and intercellular orientation of the ciliary beating plane is lacking so far in the literature. Therefore, we first of all assume that cilia belonging to a cell have a coinciding beating plane. As it is conceivable that the ciliary orientation on a cell might be more strict than between cells, the actuators can be oriented vertically or horizontally, as illustrated in Fig.1. Note that the two different possible orientations are not meant being perpendicular to each other, but to represent two distinct orientations of the ciliary beating plane differing by an arbitrary angle.

Here, we consider three different conceivable parquet-like cell alignments shown in Fig.2. In the following we shall refer to these three cell alignments as (from the left to the right according to Fig.2) unidirected square lattice (USL), unidirected hexagonal lattice (UHL) and bidirected hexagonal lattice (BHL).

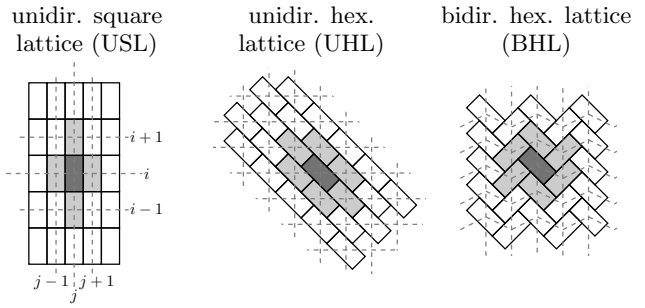

FIG. 2. Three different cell alignments have been investigated. Bright gray colored cells label the neighborhood of a central cell colored in dark gray. Dashed grid lines indicate the mapping onto a two-dimensional array.

Another important characteristic of the morphology represents the population densities of ciliated and unciliated cells, whose role for the mucociliary dynamics has not been considered so far. According to electron microscopic studies [5, 6] the area covered by ciliated cells roughly varies between one and two thirds of the total surface of the tracheal lining. Consequently, unciliated cells should be considered in pluricellular models. Therefore, we include the fraction of unciliated epithelial cells by the parameter $f \in [0, 1]$, representing the proportion of randomly distributed empty sites in an array of actuators.

Finally, as indicated by the dashed grid lines in Fig.2 the virtual epithelium is represented by a two-dimensional array. For convenience, a site located at the i-th row and j-th column is denoted as ψ_{ij}. ψ_{ij} either represents an actuator, then $\psi_{ij} \in \{0, 1\}$, or indicates an empty site representing an unciliated cell, then $\psi_{ij} = NAN$. Accordingly, the state of an array having I rows and J columns can be denoted as: $\Psi = \{\psi_{ij}\}$, where $\psi_{ij} \in \{0, 1, NAN\}$.

C. Boundary Conditions

Experiments aiming at the characterization of spatio-temporal features of mucociliary phenomena on the tracheal ciliary epithelium are based on the approach of excising a rectangular piece of the cylindric trachea (e.g. [7, 23–25]), which changes the boundary conditions from cylindrical to open. The excision might influence the collective dynamical behavior of the system. Therefore, we consider four different boundary conditions, which are illustrated in Fig.3 and shall be referenced in the following as: open boundaries (OP), vertical cylindric boundaries (VC), horizontal cylindric boundaries (HC) and toric boundaries (TO).

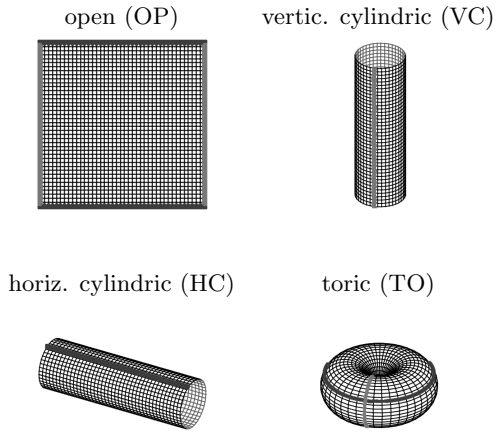

FIG. 3. Boundary conditions: open, vertical cylindrical, horizontal cylindrical and toric boundaries. The dark gray and bright gray lines indicate wrapped boundaries.

D. Mucus

Mucus is discontinuously incorporated by randomly seeding mucus droplets of equal size. On the one hand, the discrete mucus model allows to simplify mucociliary interactions. On the other hand, it accounts for the fact that the mucus blanket is anyway made up of excreted

mucus "flakes", "plaques" or "droplets" [26], which may coalesce into a continuous layer, if their density is sufficiently large [27].

According to Fig.1 each actuator provides an empty field (0 or 1), which can be occupied by mucus droplets. On the other hand, empty sites (unciliated cells) provide two fields (0 and 1), which can be occupied by mucus droplets. Thus, the distribution of mucus droplets on the virtual epithelium is given by $M = \{m_{ij}\}$; if $\psi_{ij} = NAN$, then $m_{ij} = m_{0ij} + m_{1ij}$.

E. System Update

In the course of a simulation the actuators are actuated sequentially. This means that only the state of the actuated actuator and its adjacent mucus configuration is updated while the states of adjacent actuators do not change. As soon as an actuator and its local mucus configuration has been updated, a subsequent actuator is updated for which the changes of the prior step are taken into account. We shall label the sequence of update steps by the "time" superscript t. Furthermore, $t' \doteq t/N$ labels the update of the whole network, consisting of N actuators, in the following. In the context of discrete dynamical systems such sequential update schemes are called asynchronous. An excellent overview of the impact of different update schemes on the network dynamics of random boolean networks is provided in [28, 29]. In order to distinguish the different update schemes, we shall use a slightly modified form of the terms proposed by C. Gershenson [29] (since we are not dealing with random boolean networks). We shall use the following update schemes:

- **DAU - Deterministic Asynchronous Update**
  This update mode corresponds to a pre-defined sequence, in which the nodes/cells in the lattice are addressed. Keep in mind, however, that determinism of addressing doesn't mean determinism of actuators motion. Whether an actuator moves or not depends on the mucociliary interactions, which are on a high degree stochastic, as we shall see in the proceeding sections.

- **RAU - Random Asynchronous Update**
  At each time step a single node is chosen randomly and updated. The random choice of nodes has been applied for sampling with and without replacement, as in [30]. Random sequences of nodes generated without and with replacement are denoted as RAU1 and RAU2, respectively.

- **SRAU - Semi-Random Asynchronous Update**
  The update scheme SRAU uses a wavelike activation: at each time step a strip of actuators gets addressed. Inside of each strip the actuators get addressed according to the RAU1 scheme. As the choice of the strip is predefined but inside the strips the sequence of actuators is chosen randomly, this addressing scheme has a semi-random character. This wave-like activation has been implemented for a wave traveling from the left to the right, as well as for a wave traveling from the top to the bottom, which we denote as SRAU1 and SRAU2, respectively.

- **Mimicking Purcell's Two-Hinged Low-Reynolds-Number-Swimmer**
  As non-reciprocal motions play an important role in a low-Reynolds-number environment the cell arrangement BHL has been used together with a prescribed addressing sequence of two neighboring actuators, V and H, forming the shape of an "L". The two actuators are addressed in the sequence VHVHVH, which would result in a four phase cyclic motion if the actuators were to move unhinderedly. This scheme, originally proposed by one of the authors in an essay in a popular scientific journal [31], was motivated by the "two-hinged low-Reynolds-number-swimmer", which has been introduced in [32] and is illustrated in Fig.5. The prescribed addressing sequence principally represents a special locally deterministic update scheme, as it considers the actual state of two locally coupled cells to determine which actuator will be addressed. The selection of the "L" is based on the update schemes introduced above (RAU1, RAU2, SRAU1, SRAU2 and DAU). Consequently, we actually mixed a local update scheme (prescribing the four-phase sequence of an "L") with different global update schemes (selecting which "L" to address). Settings using the coupling of two cells forming an "L", will be accounted for a cell arrangement, referred to "BHL+L".

The different update schemes have been applied in order to investigate the role of potential intercellular signaling mechanisms on the airway epithelium for the dynamical behavior of our network.

F. Local Mucociliary Interactions

Hydrodynamical interactions between adjacent ciliated cells are considered in a simplified fashion and implemented in terms of logical local decision rules induced by mucus droplets randomly seeded on the empty sites in the network. The system's evolution is achieved by attempting to move the individual actuators. As interactions between actuators occur only if mucus is located on the activated actuator, an activated actuator can switch its state unhinderedly as long as there is no mucus hindering its oscillation. In the presence of mucus, the actuator can shift and squeeze single droplets, or stacks of droplets, depending on the available energy.

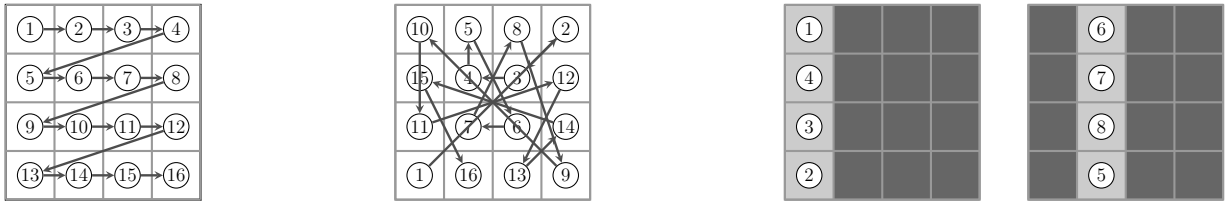

FIG. 4. The figure illustrates different update schemes for a lattice consisting of 4×4 cells. The Numbers indicate the order of activation (for one certain time step). From left to right: a pre-defined sequence (DAU), random cell selection without replacement (RAU1) and a planar wave-like activation (SRAU1).

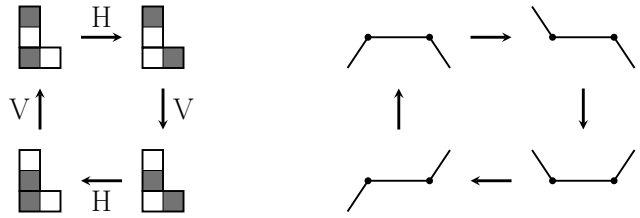

FIG. 5. The prescribed cyclic four-phase motion of two adjacent actuators forming the shape of an "L" (left). The construction of this four-phase motion-sequence was motivated by Purcell's two-hinged swimmer (right).

There are two possibilities that an activated actuator remains in its actual state. Either the active actuator has not enough energy to squeeze the mucus lumps on adjacent fields, or the actuator is situated in a locked configuration (see Fig.6).

Note that there are always two possible locked configurations for each actuator, which we shall refer to in the following as l_0 and l_1.

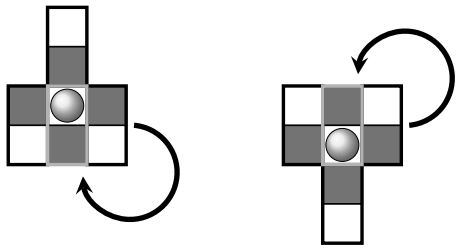

FIG. 6. In certain state configurations the active actuator (indicated by the bright surround) is locked and consequently, remains in its actual state: $\psi_{ij}^{t+1} \to \psi_{ij}^{t}$.

If the activated actuator is not situated in a locked configuration it either flips its state by squeezing the concerned mucus on adjacent fields, or it stagnates and remains in its current state (see Fig.7). The squeezing of mucus on adjacent fields is associated with a certain change of free energy. Prior to its attempt to move, an actuator gets a certain amount of energy ascribed, which has been inverse sampled. If the actuator's ascribed energy exceeds the required moving energy, the actuator is able to move. This way, the actuators' energy distribution and the situation-specific change in free energy determines the probability for an actuator to flip its state by squeezing the mucus on adjacent actuators.

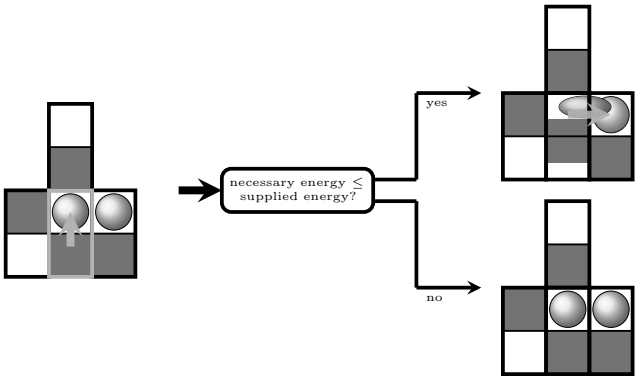

FIG. 7. If the active actuator holds a mucus lump, the actuator is either going to stagnate or it has enough energy available to squeeze the mucus lump and switch its state.

For computational purposes it is convenient to consider the mucus-free case ($m_{ij}^{t} = 0$) as a special case, in which an actuator is always able to switch its state (see Fig.8).

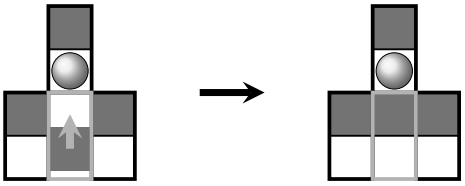

FIG. 8. An activated mucus-free actuator is always able to alternate its state.

Intercellular coordination, or rather the emergence of global spatio-temporal patterns, are caused by stagnating actuators as well as locked configurations, as in these situations the activated actuator has to adjust its state according to the local state and mucus distribution.

G. Boolean Network Representation

In this study the mucociliary dynamics on the epithelium are represented in terms of an adaptive boolean net-

work. Ciliated cells are imported in terms of boolean actuators and represent the nodes of the network. The links between nodes represent mucociliary interactions, which we formulate in terms of boolean functions.
Formally, a boolean network consists of N elements $\{\psi_1, \psi_2, ..., \psi_N\}$, each of which is a binary variable $\psi_i \in \{0, 1\}$ representing a node in the network. In general [33], the value of a node ψ_i at time $t+1$ is given as a function f_i of its K_i controlling elements at time t:

$$\psi_i^{t+1} = f_i(\psi_{j_1(i)}^t, \psi_{j_2(i)}^t ..., \psi_{K_i(i)}^t) \ . \tag{1}$$

The boolean function f_i as well as the number of controlling elements K_i may be different for each node. The dependence on node i explicitly denotes that the set of controlling nodes with indices $\{j_1, j_2, ..., K_i\}$ generally varies from one node to the other.

In our case, ψ_{ij} at time $t+1$ is given as a function f_{ij} of the local state configuration $\{\psi_{pq}\}_{pq\in n_{ij}}$ and the local distribution of mucus droplets $\{m_{pq}\}_{pq\in n_{ij}}$ at time t:

$$\psi_{ij}^{t+1} = f_{ij}\big(\{\psi_{pq}^t\}_{pq\in n_{ij}}, \{m_{pq}^t\}_{pq\in n_{ij}}\big) \ . \tag{2}$$

The neighborhood n_{ij} of the actuator ij is illustrated in Fig.2. The function f_{ij}, i.e. representing the local mucociliary interactions, imports the actuators' available energy and will be specified in Sec.II H.

The oscillatory driving force of ciliated cells results in the permanent attempt of a node for state reversal and is represented by the logical XOR-function:

$$\psi_{ij}^{t+1} = \mathrm{XOR}(\psi_{ij}^t, c_{ij}^t) \ . \tag{3}$$

Here $c_{ij}^t \in \{0, 1\}$ represents the local couplings among the nodes. If $c_{ij}^t = 1$, that is if the actuator is capable of displacement, then the XOR-function inverts an actuator's actual state ψ_{ij}^t. On the other hand, if the actuator is situated in a locked configuration (Fig.6) or stagnates due to an excessive mucus load (Fig.7), then c_{ij}^t gets false/zero and consequently, remains in its current state.

The actuator is capable of displacement if it's not blocked and if the free energy u available to the actuator is larger than the work Δw needed to displace the mucus. Thus, we write the condition for a state alternation as:

$$c_{ij}^t = \mathrm{NOR}(l_0, l_1) \cdot \Theta\big[u - \Delta w\big] = 1 \ . \tag{4}$$

l_0 and l_1 denote the two locked state configurations (Fig.6) and $\Theta(x)$ the Heaviside step function, such that $\Theta(0) = 1$.

In order to clarify the state alternation condition we shall reconstruct the intuitively formulated local interactions, which have been illustrated in Fig.6-Fig.8:

- Fig.6: In locked configuration case, either $l_0 = 1$ or $l_1 = 1$ and consequently, $\mathrm{NOR}(l_0, l_1) = 0$. As $c_{ij}^t \sim \mathrm{NOR}(l_0, l_1)$, the activated actuator remains in its current state.
- Fig.7: In hindered motion case $\mathrm{NOR}(l_0, l_1) = 1$ and thus the condition for state alternation reads (according to Eq.4): $u \geq \Delta w$.
- Fig.8: Obviously, mucus-free actuators are not locked and consequently: $l_0 = l_1 = 0 \implies NOR(l_0, l_1) = 1$. As there is no mucus to redistribute the required work vanishes ($\Delta w = 0$) and thus, the state alternation occurs spontaneously.

It is important to realize that the distribution of mucus droplets determines the topology of the network, as the update of mucus-free nodes is not affected by their local environment. As soon as an actuator gets occupied by a mucus droplet, it gets functionally connected to its neighboring nodes, as its subsequent state depends on the local state and mucus configuration. Consequently, in our network not only the network's state is exposed to dynamics, but also the network's topology, as the (re-)distribution of the droplets depends on the state transitions of the nodes and vice versa. Networks exhibiting such a feedback loop between the network's state and its topology are called coevolutionary or adaptive networks [34].

H. Actuator-Energy and Mucus Relaxation

The interactions are quantified using a simple scheme intended to model in a crude fashion the transient entropic elasticity and relaxation of entangled mucin chains. We view the actuator as a piston acting against the pressure p exerted by mucus droplets contained in a certain volume V. For simplicity we assume that the interactions are mediated only through the set of n direct neighbors of the targeted site. As a result the volume to be compressed by the action of the piston is $V = n\Delta V$ (see Fig.9). By moving the actuator, this volume changes

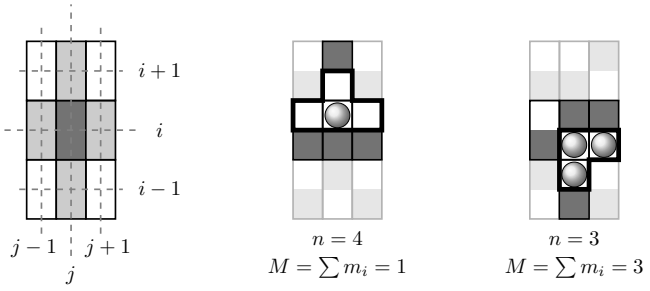

FIG. 9. The left panel illustrates the neighborhood of actuators aligned in the square-lattice. Bright gray actuators control the subsequent state of the actuated dark gray actuator. Middle and right panel: Two situations which are thought to illustrate the locally concerned volume $V = n\Delta V$ and the involved number of mucus droplets M. Bleached actuators are not involved to the current interaction.

by $-\Delta V$ to $V' = (n-1)\Delta V$, what requires the work $\Delta w = p\Delta V$. (Strictly speaking we should consider the

pressure difference $\delta p = p_f - p_b$ between the front and back of the actuator. We apologize for forgetting the back pressure p_b in the present set of simulation data, what fortunately does not change the main conclusions.)

To determine the pressure p we employ the standard thermodynamic relation: $p/T = \partial S(V)/\partial V$, where $S(V) = k_B \ln(W_V)$ is the Boltzmann entropy of the mucus droplets enclosed within V. Replacing the differentials by discrete differences $\partial S \to \Delta S = k_B \ln(W_{V'}/W_V)$ and $\partial V \to -\Delta V$ yields

$$\Delta w = p\Delta V = k_B T \ln\big(\frac{W_n}{W_{n-1}}\big) \ . \tag{5}$$

Subsequently, we set $k_B T = 1$, i.e., energy is measured in units of $k_B T$. A plausible expression for the multiplicity ("thermodynamic probability") W_n can be deduced as follows: Random deposition of M mucus droplets on n available sites is equivalent to rolling an n-sided dice. Thus, the result of the deposition of M droplets is a sample from the multinomial distribution, with equal probabilities for hitting a field unoccupied by an actuator. Thus, the multinomial coefficient $C_m = M!/(m_1! m_2! \cdots m_n!)$ is a good candidate for the multiplicity in Boltzmann entropy. (m_i denotes the number of droplets deposited on a site i.) However, after the deposition, prior to an attempted move of an actuator, we allow the distribution of droplets to relax to a "thermodynamic equilibrium", i.e., into a state of maximum multiplicity, where the droplets are most uniformly distributed on the available sites, so that $|m_i - m_j| \leq 1$, for $i \neq j$. (In other words, we invoke the Maximum Entropy Principle [35].) Therefore, we define the multiplicity involved in Eq. 5 as $W_n = \min\big(m_1! m_2! \cdots m_n!\big)$ and $W_{n-1} = \min\big(m_1'! m_2'! \cdots m_n'!\big)$, where m_i and m_i' are subject to the constraints $\sum_{i=1}^{n} m_i = \sum_{i=1}^{n-1} m_i' = M$.

To complete the specification of the mucociliary interactions we must specify the actuators energy u. At this point we introduce an additional stochastic element, assuming a certain distribution $f_U(u)$ of the actuator energy. Prior each attempt an actuator's energy u is obtained by reverse sampling, according to: $u = F_U^{-1}(r)$, where r represents a uniformly distributed random number and F_U the cumulative energy distribution. Since a cumulative distribution is a monotonous function of its argument, the sampling can be concisely included into the boolean update equation for c_{ij}^t as:

$$\psi_{ij}^{t+1} = \mathrm{XOR}\big\{\psi_{ij}^t, \mathrm{NOR}(l_0, l_1) \cdot \Theta\big[r - F_U(\Delta w)\big]\big\}. \tag{6}$$

In the present simulations we used (for certain "historical reasons") the simple expression

$$F_U(u) = \frac{1}{\frac{\epsilon}{1-\epsilon}\exp(-u) + 1} \ , \tag{7}$$

where $u \geq 0$ and ϵ parameterizes the actuators' energy supply. This function is illustrated in Fig.10.

Finally, we summarize the update of an actuator's state and its local mucus configuration in the form of a flow chart in Fig.11.

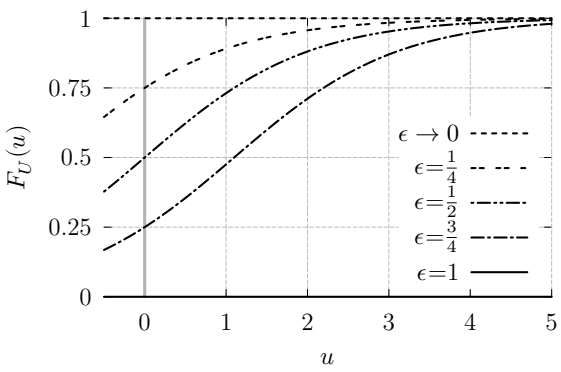

FIG. 10. The curves show the actuators' cumulative energy distribution for different values of the energy parameter: $\epsilon \in \{\frac{1}{4}, \frac{1}{2}, \frac{3}{4}, 1\}$ and for $\epsilon \to 0$.

III. SIMULATIONS AND RESULTS

A. Initial State

Prior to simulation the state of the virtual epithelium has to be initialized. First, an array of N actuators with random states is generated, i.e. Ψ^0, where $\psi_{ij} \in \{0, 1\}$ are uniformly distributed. Second, as the fraction f represents the number of unciliated cells, $f \cdot N$ randomly chosen sites are set to NAN. A certain amount of mucus droplets is then seeded on a randomly chosen site (uniformly distributed). For the sake of comparability between open and toric boundary conditions the amount of mucus droplets was held constant during the simulation. Therefore, when applying open boundaries the mucus droplets leaving the modeling area were reefed on a randomly chosen site. This way, we principally assumed the mucus excretion to be proportional to the mucus transport, which would of course need some kind of internal regulation mechanism in a real trachea.

B. Parameter Study

In order to assess under which circumstances our model self-organizes towards a self-cleaning virtual epithelium and how it reaches its properly functioning states dynamically, the influence of the model parameters, introduced in the previous chapter, on the network dynamics has been studied. The main parameter study encompasses the variation of the six model parameters in the following ranges. All cell alignments (USL, UHL, BHL, BHL+L), all update schemes (DAU, RAU1, RAU2, SRAU1, SRAU2) and all boundary conditions (OP, HC, VC, TO) have been used. The amount of mucus lumps has been varied in the range of 0.5%, 1%, 2%, 4%, ..., 256% of the total number of actuators in the grid (an amount of 4% corresponds to $0.04 \cdot N$ mucus droplets). The amount of unciliated cells has been set to 0%, 5%,

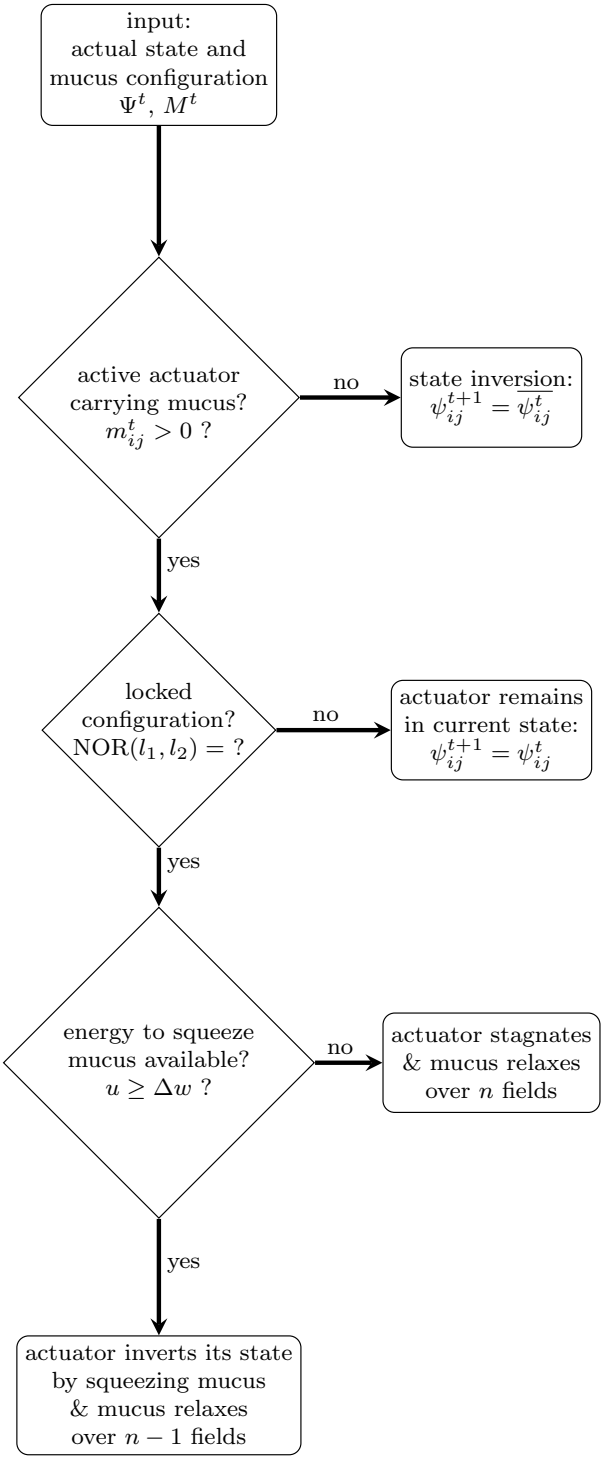

FIG. 11. The flow chart illustrates the update of an actuator's state as well as its local mucus distribution.

10%, 15%, 20%, 25% and finally, the energy parameter has been set to 0, 0.25, 0.5, 0.75 and 1. Consequently, our main parameter study encompasses 24'000 simulation runs, which have been iterated for 10^5 time steps using a grid size of 50×50 cells. These simulations can be seen as a starting point of further simulations we conducted. Each simulation run is characterized by its corresponding parameter setting. A specific parameter set is denoted as a combination of the form: (grid size, cell alignment, update scheme, boundary condition, mucus amount, energy parameter, amount of unciliated cells).

C. Observables

To provide a qualitative impression of the self-organizing character of the network model and to illustrate the meaning of the chosen observables, we present first a typical simulation run. The parameters have been set to (50×50, USL, DAU, TO, 16%, 0.5, 0%). Fig.12 shows the state of the network at three different stages of the self-organization process. Fig.12 represents a substitute for the temporal evolution of the network's state, which is best visualized by movie_S1 (see supplemental material [36]). Actuators are colored in dark gray if $\psi_{ij}^t = 1$ or in bright gray if $\psi_{ij}^t = 0$. Mucus lumps are shown in white. Fig.12a shows the initial network state displaying the randomly generated initial configuration of states and mucus lumps. Fig.12b visualizes the state of the network after 100 iterations, representing an intermediate stage of the self-organization process, as the emergence of global order becomes clearly visible. Finally, Fig.12c shows the network state after 1500 iterations. At this stage the fascinating self-organization process has almost completed, and the actuators finally behave strongly coordinated at a global scale. By examining the successive network states in movie_S1, one can observe that the particles get initially moved around disorderly. Quickly, the actuators start to cooperate by adjusting their oscillations to the oscillations of the surrounding actuators until the particles get efficiently transported into a well defined direction - what we call self-organized transport. Consequently, in our models the self-organization process is actually twofold. As in accordance with the emergence of spatio-temporal patterns, the virtual epithelium exhibits self-organized transport. This co-evolution of the network state and its associated mucus transport has been quantified in terms of several observables, which are introduced in the following.

1. *Mucus Transport Velocity*

For each actuator at the position ij at time t we assign a local mucus velocity in terms of the local displacement of the center of mass (CM), which we denote as $\vec{v}_{ij}(t)$ and has been calculated (if $m_{ij}^t > 0$) according to:

$$\vec{v}_{ij}(t) \doteq \frac{\sum_{p,q \in n_{ij}} (\vec{r}_{ij} - \vec{r}_{pq})(m_{pq}^{t+1} - m_{pq}^t)}{\sum_{p,q \in n_{ij}} m_{pq}^t} \qquad (8)$$

$\vec{v}_{ij}(t)$ measures the redistribution of mucus droplets in the neighborhood n_{ij} of the activated actuator at ij in

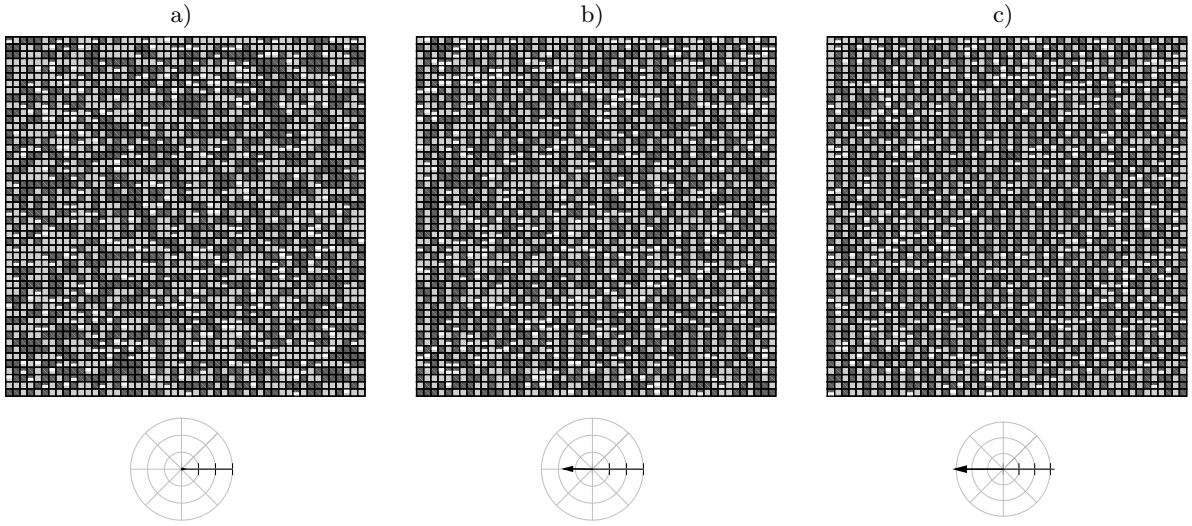

FIG. 12. The panels show the network state of an exemplary simulation run at three different stages of the self-organization process. The three crosshairs in the second row visualize the magnitude and the direction of the mucus transport velocity $\vec{v}_g(t')$ at each stage (the radial tick interval corresponds to 0.2 [cells/it]. a) initial network state: randomly distributed states. b) network state after 100 iterations: due to the local interactions the emergence of order becomes visible. c) after 1500 iterations: the self-organized cooperative behavior of actuators forms spatio-temporal patterns and exhibits efficient self-organized transport.

terms of the local displacement of the CM. $\vec{r}_{ij} - \vec{r}_{pq}$ denotes the distance vector pointing from the activated actuator at ij to the neighboring actuators at pq. This relative distance vector gets weighted by the redistributed mucus droplets $(m_{pq}^{t+1} - m_{pq}^{t})$.
In order to quantify the global transport velocity $\vec{v}_g(t')$ (remind that $t' \doteq t/N$) we calculate the mucus-weighted average over the whole array of actuators of the formerly defined local velocity of the CM in Eq.(8) according to:

$$\vec{v}_g(t') \doteq \frac{\sum_{ij} \vec{v}_{ij}(t') \sum_{p,q \in n_{ij}} m_{pq}^{t'}}{\sum_{ij} \sum_{p,q \in n_{ij}} m_{pq}^{t'}} \ . \qquad (9)$$

$\vec{v}_g(t')$ represents an approximation to the actual average mucus transport velocity, as droplets moving more than one field in one single timestep are neglected. As these movements only happen due to fluctuations originating from mucus relaxation, $\vec{v}_g(t')$ represents a good measure for the area averaged mucus transport velocity. Fig.13 shows the temporal evolution of the global mucus transport speed $|\vec{v}_g(t')|$ for an ensemble consisting of 100 simulation runs differing only by their initial state. Each ensemble member corresponds to a simulation run for which the parameter setting (50×50, BHL+L, RAU1, OP, 10%, 1, 0%) has been used. The curve shows the temporal evolution of the ensemble mean (solid line) and its standard deviation (shaded area) and displays the typical saturation-like behavior of the average mucus transport speed, which has been observed for any parameter setting showing a self-organizing behavior. Accordingly, we can define the initial mucus transport velocity $\vec{v}_{g0} \doteq \lim_{t' \to 0} \vec{v}_g(t')$ and the final mucus transport velocity $\vec{v}_{g\infty} \doteq \lim_{t' \to \infty} \vec{v}_g(t')$. Consequently, the global average transport velocity can be expressed as

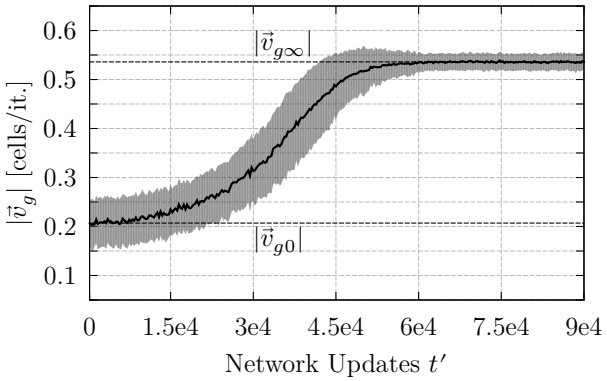

FIG. 13. Temporal evolution of the average mucus transport speed of an ensemble consisting of 100 simulation runs. The typical limited growth behavior was omnipresent in all of our simulation runs displaying a self-organizing behavior.

$$\vec{v}_g(t') = \vec{v}_{g0} + (\vec{v}_g(t') - \vec{v}_{g0}) \doteq \vec{v}_{g0} + \Delta\vec{v}_g(t') \ , \qquad (10)$$

where $\Delta\vec{v}_g(t')$ can be seen as the effectively self-organized mucus transport velocity.

2. Mucus Transport Direction

We observed that some parameter settings drive the model towards strongly ordered attracting network states

exhibiting non-negligible area averaged transport speeds. In some of these strongly ordered states the direction of transport varies with the grid location. Consequently, in order to be able to classify the parameter settings into functioning and malfunctioning settings, we quantified the mean transport direction in terms of $\langle \cos\theta \rangle$ defined as:

$$\langle \cos\theta \rangle \doteq \sum_{ij} \cos\theta_{ij}, \text{ where } \theta_{ij} \doteq \lim_{t' \to \infty} \frac{\vec{v}_{ij}(t') \cdot \vec{v}_g(t')}{|\vec{v}_g(t')| \cdot |\vec{v}_{ij}(t')|} . \tag{11}$$

Fig.14 depicts an example of an ordered attracting network state (upper panel) exhibiting a disordered velocity field (lower panel). The illustrated example has been generated by applying the parameter set (50×50, UHL, DAU, OP, 64%, 1, 0%). The displayed attracting state exhibits a global average velocity of $\vec{v}_{g\infty} = (-0.14, -0.03)$ [cells/it.]. The corresponding initial transport speed $|\vec{v_0}|$ amounts to 0.1 [cells/it.]. The autocorrelation length ρ_c amounts to 3.4 cells. As the parameter sets shall be classified as functioning and malfunctioning, $\langle \cos\theta \rangle$ was used to exclude states showing such a poorly defined transport direction as the one shown in Fig.14, for which $\langle \cos\theta \rangle = 0.18$.

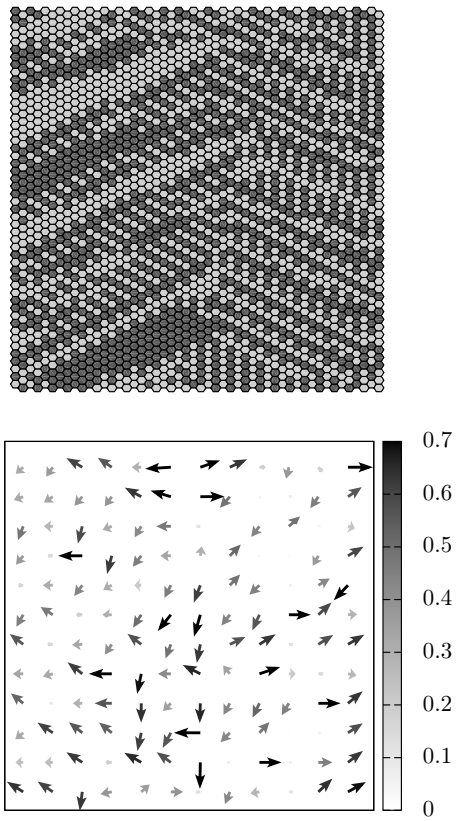

FIG. 14. Example of a highly ordered attracting state (top) as well as self-organized transport, but displays a disordered (temporally averaged) velocity field (bottom). The gray level indicates the droplets' speed [cell/it.].

3. *Transient Time*

Since $\Psi^{t'}$ represents the state of the Boolean network at time t' containing N Boolean variables, the set of all 2^N possible network states forms the state space of the Boolean network. The successive network states Ψ^0, Ψ^1, Ψ^2... form a trajectory in the state space. In the case of deterministic Boolean networks, a network sooner or later reaches a state, which has been reached before (due to the finite state space) and consequently, enters a cycle consisting of a subset of states of the state space, which is called an attractor. A more general definition for dynamical systems says that an attractor is a set of states to which the system evolves after a long enough time [37]. The transient time τ is the number of states a network undergoes (starting from an initial state), before it reaches an attractor [38–40].

Fig.15 depicts the temporal evolution of two ensembles consisting of 100 ensemble members differing only by their initial condition. The brighter band corresponds to the curve presented in Fig.13 showing the evolution of the average mucus transport speed being generated with the parameter setting (50×50, BHL+L, RAU1, OP, 10%, 1, 0%). The darker curve has been generated with exactly the same parameter settings apart from the update scheme. Instead of RAU1 the update DAU was used. Both ensembles show the typical saturation-like temporal evolution of the average transport speeds, which reflects the capturing of the system dynamics by attractors. We calculated the transient time based on the transient behavior of the average transport speed, which roughly follows an exponential behavior: $|\vec{v}_g(t')| = |\vec{v}_{g0}| + \exp(-t'/\tau') \cdot (|\vec{v_{g\infty}}| - |\vec{v_0}|)$. The transient time τ has been defined as $\tau \doteq 3 \cdot \tau'$. As one can notice in Fig.15 the transient time for the ensemble simulation using the deterministic update scheme DAU is roughly four times shorter than the one for which the update scheme RAU1 was used. This behavior may be more fundamental and shall be discussed later.

4. *Autocorrelation*

In order to characterize the coordination amongst the actuators in a particular network state, we use the spatial autocorrelation function $C(\Delta i, \Delta j, t') = \sum_{i,j} \Psi(i,j,t')\Psi(i+\Delta i, j+\Delta j, t')$, where Δi and Δj denote the shifts into the i- and j-direction, respectively. As we would like to compare different simulation runs with respect to the emergent spatial order, we used the autocorrelogram to determine the spatial autocorrelation-length ρ_c, representing a measure for the degree of order in a network state. As most correlograms appear

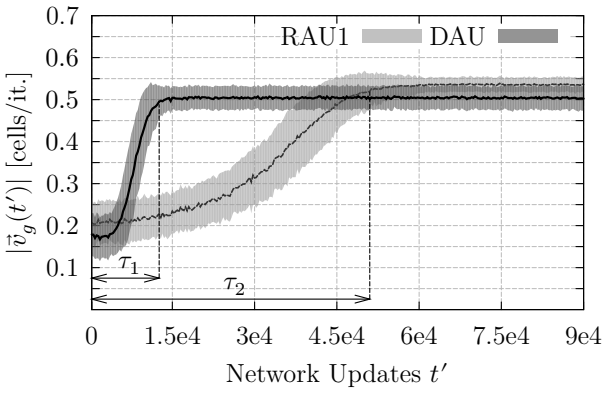

FIG. 15. The curves show the temporal evolution of the average mucus speed for two ensemble simulations differing only by their update scheme. The darker and brighter curve correspond to simulations for which DAU and RAU1 has been applied, respectively. Simulation runs initialized with the update scheme DAU reach roughly four times faster their attractors than those initialized with RAU1, which is indicated by the corresponding transient times τ_1 and τ_2.

to be strongly elongated as illustrated in Fig.16, we determined the autocorrelation-length along the direction of maximum correlation, which is indicated by the gray plane in Fig.16. Note that in roughly 95% of all properly self-cleaning attracting states the direction of maximum correlation coincides with the direction of mucus transport. As most correlograms show an exponential-like decrease along the direction of maximum correlation, the autocorrelation-length ρ_c has been determined according to:

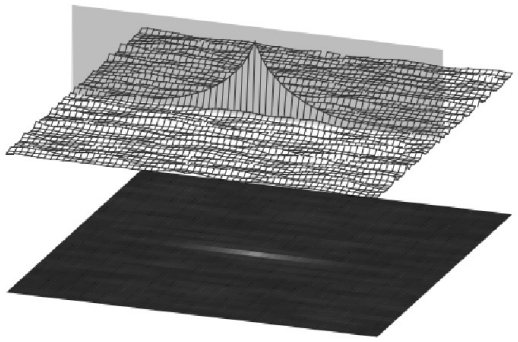

FIG. 16. The autocorrelograms of attracting states typically have an elongated shape along a certain direction (indicated by the bright gray vertical plane), along which we determined the autocorrelation-length ρ_c.

$$\rho_c(t') = \max\left\{ \frac{1}{2} \sum_{v=v_1 \ldots v_2} \mathrm{C}(v, \gamma(v), t') \;\; | \;\; \gamma(v) = a \cdot v + b \;;\; a, b, v \in \mathbb{R} \;;\; 0 \leq v_1, v_2 \leq I; 0 \leq \gamma(v) \leq J \right\} \tag{12}$$

Eq.12 delivers the autocorrelation-length ρ_c along the line of maximum correlation, which is represented by the parameterization $\gamma(v)$.

D. Co-evolution of Spatio-Temporal Patterns and Transport

The co-evolution of self-organized transport and spatio-temporal patterns is illustrated in Fig.17. The brighter curve shows the area-averaged transport speed $|\vec{v_g}(t')|$ (according to Eq.9) illustrating the build up of self-organized transport. The darker curve represents the auto-correlation length of the network's state at time t'. As at the beginning of the simulation the mucus droplets get displaced almost erratically, the corresponding area-averaged transport speed almost vanishes. As time passes the average particle speed grows until the coordination of the actuators reaches a maximum. The three vertical dashed lines indicate the moments at which the three network states shown in Fig.12 have been recorded. Interestingly, all model settings leading to self-organized transport have shown a similar growth behavior with respect to the global average transport speed as the one depicted in Fig.17. This typical transient dynamical behavior reflects the restricted growth of the cooperation among the actuators. This sigmoid logistic-like dynamical behavior can be observed in other studies inves-

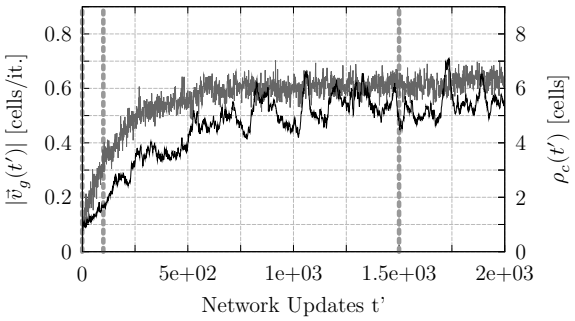

FIG. 17. The graph illustrates the co-evolution of the autocorrelation length of the network state along the direction of maximum correlation $\rho_c(t')$ (dark curve) and the area averaged mucus transport speed $|\vec{v_g}(t')|$ (bright curve).

tigating self-organizing processes as well, and appears to be omnipresent for self-organizing processes. An example is provided by Fig.2 in [41], in which the self-organized synchronization and wave formation in one-dimensional cilia arrays has been studied.
Within the meaning of the state space concept, the curves in Fig.17 can be seen as the network's transient behavior. The saturation-like behavior reflects the capture of the network dynamics by an attractor. Accordingly, the strongly ordered network state shown in Fig.12 represents an attracting state.

Our model typically exhibits a co-evolution of the network's state and its associated mucus transport. As indicated earlier, we suggest to see this two-fold self-organization in the context of adaptive boolean networks. Since mucus droplets functionally connect an actuator to its surrounding and disconnect an actuator when squeezed away, the network topology is exposed to dynamics and interrelated to the dynamics of the network's state. Consequently, we observe not only dynamics *on the network*, represented by state transitions, but also *dynamics of the network*, caused by the transportation of the mucus droplets. This means that changes in the network's state are affected by the network's topology and vice versa, forming a feedback loop between the topology and the state of the network. The resulting co-evolution of the network state and the network topology represents the characteristic property of coevolutionary or adaptive (boolean) networks [34, 42].

E. Update Schemes

In this section we discuss the influence of the different update schemes, introduced in Sec.II E, on the system dynamics of our model.

1. *Which Parameter Settings Drive The Model Towards a Self-Organized Self-Cleaning State?*

In order to get an overview of which parameter sets show a higher probability for a self-organization towards properly self-cleaning states, the parameter settings were classified as "functioning" and "malfunctioning". A certain parameter setting is classified as functioning, if the following four conditions are simultaneously fulfilled after an integration time of $t' = 10^5$. 1) The globally averaged transport speed $|\vec{v}_{g\infty}|$ is faster than 0.1 cells/it., which roughly corresponds to $20\mu m/s$ in the real system (assuming a ciliary beat frequency of 10 Hz and the diameter of a ciliated cell being 10μm). 2) We require the velocity field being sufficiently directed by: $\langle \cos\theta \rangle > 0.65$. 3) The velocity field must be self-organized and not simply being imposed by the choice of a parameter set leading to an initial tendency of the transport direction. Consequently, by requiring $|\Delta\vec{v}| \doteq |\vec{v_{g\infty}} - \vec{v_{g0}}| > 0.1$, we demand that the velocity field changes (at least its direction) in the course of a simulation. 4) The auto-correlation length ρ_c has to be longer than two cells. The number of iterations may be seen as a fifth condition considering the efficiency of the self-organization process. As thus, the transient time τ has to be shorter than 10^5 iterations. The classification of parameter sets as functioning and malfunctioning was applied to the parameter study encompassing 24'000 parameter sets. 564 out of 24'000 settings ($\widehat{=}$ 2.4%) have been classified as functioning. Table I shows how these functioning settings spread across the different cell alignments and update schemes (values are listed in [%]). Table I summarizes the following observations. The cell alignment USL can cope with the largest set of parameter settings and makes up 84.2% of all functioning settings. 98.2% of all functioning settings are made up by settings using either the cell alignment USL or BHL+L. The deterministic update scheme DAU can cope with each cell alignment and 89.6% of all functioning settings were generated by this update scheme. None of the settings using the completely random update RAU2 evolves the network to a self-organized self-cleaning state. The cell alignment BHL+L (lowest row in table I) can cope with all update schemes except the fully random update scheme RAU2. Apparently, a certain degree of local pre-coordination, as it results from the particular local deterministic update scheme (Sec.II E), is advantageous for an efficient self-organization. This observation reveals a possibly more fundamental behavior, which has been analyzed in more detail and is going to be highlighted in the following section.

TABLE I. The table shows how the functioning states spread across the different topologies and update schemes. The values represent the corresponding proportions of all functioning states in [%].

	DAU	RAU1	RAU2	SRAU1	SRAU2
USL	84.2	0.0	0.0	0.0	0.0
UHL	1.2	0.0	0.0	0.0	0.0
BHL	0.5	0.0	0.0	0.0	0.0
BHL+L	3.7	1.6	0.0	0.9	7.8

2. *Imposed Asymmetry as a Starting Assistance For Self-Organized Self-Clearing*

In this section we discuss the potential role of imposed asymmetries as a control parameter. As shown in Table I functioning settings either include DAU or BHL+L, or both - all other settings don't result in self-organized self-clearing states. Consequently, these settings may reveal a common characteristic which ultimately leads to self-organized self-cleaning. We realized that properly functioning parameter sets consistently impose an initial tendency of the transport direction. The initial area averaged transport speed $|\vec{v}_0|$ can be used in order to

quantify the anisotropy of the transport at time t'=0. In order to estimate the expected initial transport speed at t'=0 of a certain parameter setting, we used a grid consisting of 1500×1500 actuators, which have been updated for a single timestep ($\Psi^0 \rightarrow \Psi^1$). This has been done for an ensemble of 100 simulation runs. The ensemble mean provides an estimate for the imposed initial transport speed $|\vec{v}_0|$. The most direct way to visualize the effect of $|\vec{v}_0|$ on the self-organizing behavior of the network is to divide the parameter settings into classes considering the values of $|\vec{v}_0|$ and to count the frequency of functioning parameter settings in each class. Fig.18 depicts the relative amount of functioning settings considering 14 $|\vec{v}_0|$-classes, whose class widths have been chosen logarithmically in the interval $[10^{-5}, 1]$. The relative

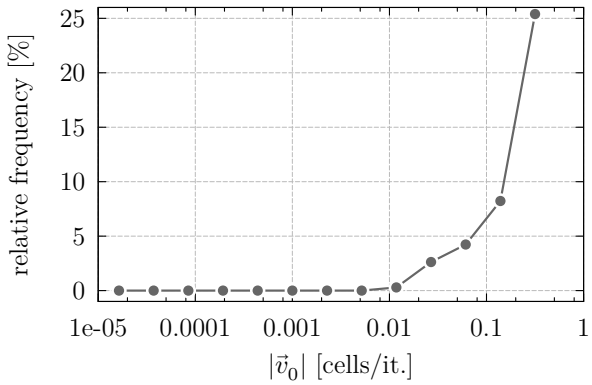

FIG. 18. The relative frequency of settings generating properly self-organized self-cleaning states increases with increasing intial transport speeds $|\vec{v}_0|$.

frequency of functioning settings clearly increases with increasing $|\vec{v}_0|$. Moreover, all functioning settings correspond to $|\vec{v}_0|$-values being faster than 0.01 cells/it. Furthermore, the measures $|\Delta\vec{v}|$, ρ_c, $\langle\cos\theta\rangle$ and $|\vec{v_\infty}|$ classifying the parameter sets tend to increase with increasing values of $|\vec{v}_0|$, as shown in Fig.19. Whiskers have been set in order to indicate the range covered by 95% of all values, outliers are suppressed. Consequently, Fig.18 and

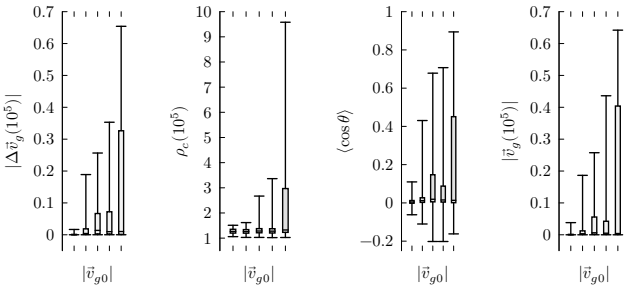

FIG. 19. Box plot diagrams indicating the increase of $\Delta|\vec{v}|_\infty$, ρ_c and $\langle\cos\theta\rangle$ with increasing $|\vec{v}_0|$. The ticks on the ordinate correspond to the following intervals: $[10^{-5}, 10^{-4}]; [10^{-4}, 10^{-3}]; [10^{-3}, 10^{-2}]; [10^{-2}, 10^{-1}]; [10^{-1}, 1]$.

Fig.19 indicate that $|\vec{v}_0|$ may trigger the model towards self-organized self-clearing.

In order to clarify which model parameters determine the value of $|\vec{v}_0|$, the boxplots in Fig.20 display how the $|\vec{v}_0|$ values distribute over the update schemes and cell alignments, corresponding to Table I. One can see that the highest values for $|\vec{v}_0|$ are reached by settings using DAU or BHL+L. This clearly suggests that update schemes with local determinism impose an asymmetry among the local interactions, what triggers efficient self-organization towards self-clearing states.

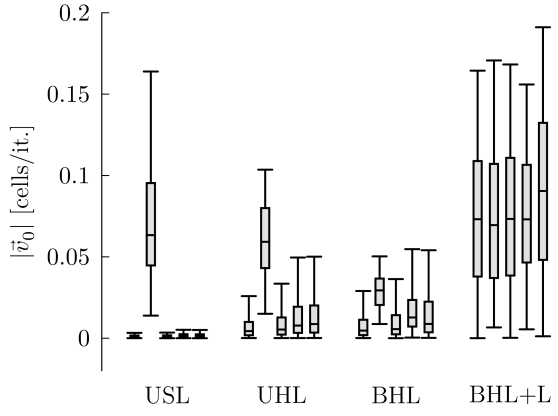

FIG. 20. Box plot diagrams to visualize the effect of the choice of the cell alignment and the update scheme on the initial transport speed. The box plots of each cell alignment correspond to the respective update scheme, according to the order: RAU1, DAU, RAU2, SRAU1, SRAU2.

3. *Effect of The Update Scheme on The Network Dynamics*

As settings using the locally prescribed four-phase sequence (BHL+L) can cope with each update scheme, we compared the dynamic behavior produced by the different update schemes by simulating an ensemble of 100 simulation runs using the parameter settings: (50×50,BHL+L, ∗, OP, 10%, 1, 0%), where ∗ ∈ {DAU, RAU1, SRAU1, SRAU2}. Fig.21 shows the transient behavior for the average mucus transport speed of the four ensembles corresponding to the different update schemes. Each setting produces a saturation-like behavior reflecting the capturing of the dynamics by attractors. As one can see, settings using SRAU2 and DAU reach their attractors considerably faster than settings using SRAU1 and RAU1. In order to characterize the state space corresponding to each setting, we counted the number of attractors and the attractor periods. It turned out that each attractor has a period of four, corresponding to the prescribed cyclic four-phase sequence. Furthermore, SRAU2 and RAU1 drive each of the 100 different initial conditions towards the same attracting state, which is

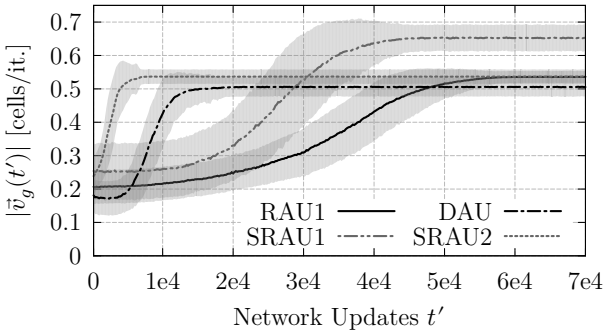

FIG. 21. The curves depict the temporal evolution of the average transport speed for four ensembles corresponding to different update schemes for which the cell alignment BHL+L was chosen.

shown in Fig.22. DAU and SRAU1 produce more realistic dynamics, as the 100 simulation runs were driven towards 90 and 95 different attracting states, respectively. For DAU and SRAU1 two exemplary attracting states are depicted in Fig.22. Even if SRAU1 drives different initial conditions towards different attracting states, the attracting states strongly resemble each other, as indicated in Fig.22. DAU produces more different emerging structures. In order to verify this observation, we ran 5 simulation runs for each update scheme, which differed by their initial state. But this time we prescribed how much their initial state shall differ against a reference run. Namely, we switched the state for 1%, 2%, 3% and 4% of all actuators, respectively, and compared the networks' state at each timestep to the reference run in terms of the normalized Hamming distance [1] (see e.g. [37]) see Fig.23). The average Hamming distance corresponding to SRAU2 and RAU1 decreases to zero, which means that all states reach the same attractor. On the other hand, SRAU1 and DAU produce different attractors, but the attractors produced by DAU show an almost maximum Hamming distance. This behavior reflects the ability of the system to find new attractors in case of a perturbation and to conform to changes, which is an important characteristic for living systems. Consequently, if an attractor which has been reached by applying DAU gets perturbed, the system conforms to changes and runs into a new attractor.

F. Effect of Boundary Conditions & Unciliated Cells

In this section, we document what general properties can be observed when varying the boundary conditions and how unciliated cells affect the self-organization process. Note that the network topology is predominantly determined by the choice of the cell alignment, the proportion of ciliated cells and the boundary conditions. Consequently, the observations of the effects of the boundary conditions and the amount of ciliated cells can't be strictly separated as they interfere, which is outlined in the following.

1. Open Boundaries: Marginal Nodes Guiding The Structure Emergence

First of all we consider a completely dense carpet of ciliated cells represented by a parquet of actuators. In this "densely ciliated carpet case" we observe that settings with open boundaries yield a structure emergence always starting at the same open boundary, from which it spreads over the whole network. This behavior is illustrated in Fig.24, where three snapshots of the network state at three different stages of the self-organizing process are shown. The graphs have been generated by applying open boundaries, RAU1 and BHL+L. Further, we observed that settings leading to the "crystallization-process", shown in Fig.24, only show this self-organizing behavior as long as the boundary, from which the structure spreads, is open. This means that similar network dynamics have been observed for open and horizontal cylindrical boundaries. On the other hand, if we chose toric or vertical cylindrical boundaries, for which the "structure-triggering" border is glued to the opposing border, the model displays a completely different dynamical behavior with much lower self-organized transport speeds and much less well ordered network states. The only exception is given by the settings using the square-lattice alignment, which shows self-organized directed transport under each boundary condition.

movie_S2, movie_S3 and movie_S4 (provided as supplemental material [36]) illustrate the structure emergence from an open boundary. They have been generated by applying (50×50, USL, DAU, OP, 10%, 0, 0%), (50×50, BHL+L, DAU, OP, 15%, 1, 0%) and (50×50, BHL+L, RAU1, OP, 15%, 1, 0%), respectively.

2. Leaders and Followers

Since we observed for the "densely ciliated carpet case" when using open boundaries that the emergence of highly ordered structures always sets in from the same boundary, the actuators at the boundary seem to play an important role for the self-organizing process and consequently, it appears that there exists a kind of hierarchy among the actuators.
This hierarchy among the nodes is caused by the underlying network topology and is primarily characterized by the distribution of in- and out-degrees. In Fig.25 we illustrate the underlying network topology for an array con-

[1] Oscillations of 0.5 in the normalized Hamming distance (caused by the XOR-function and the BHL+L setting) are suppressed by taking the minimum of four consecutive Hamming distances.

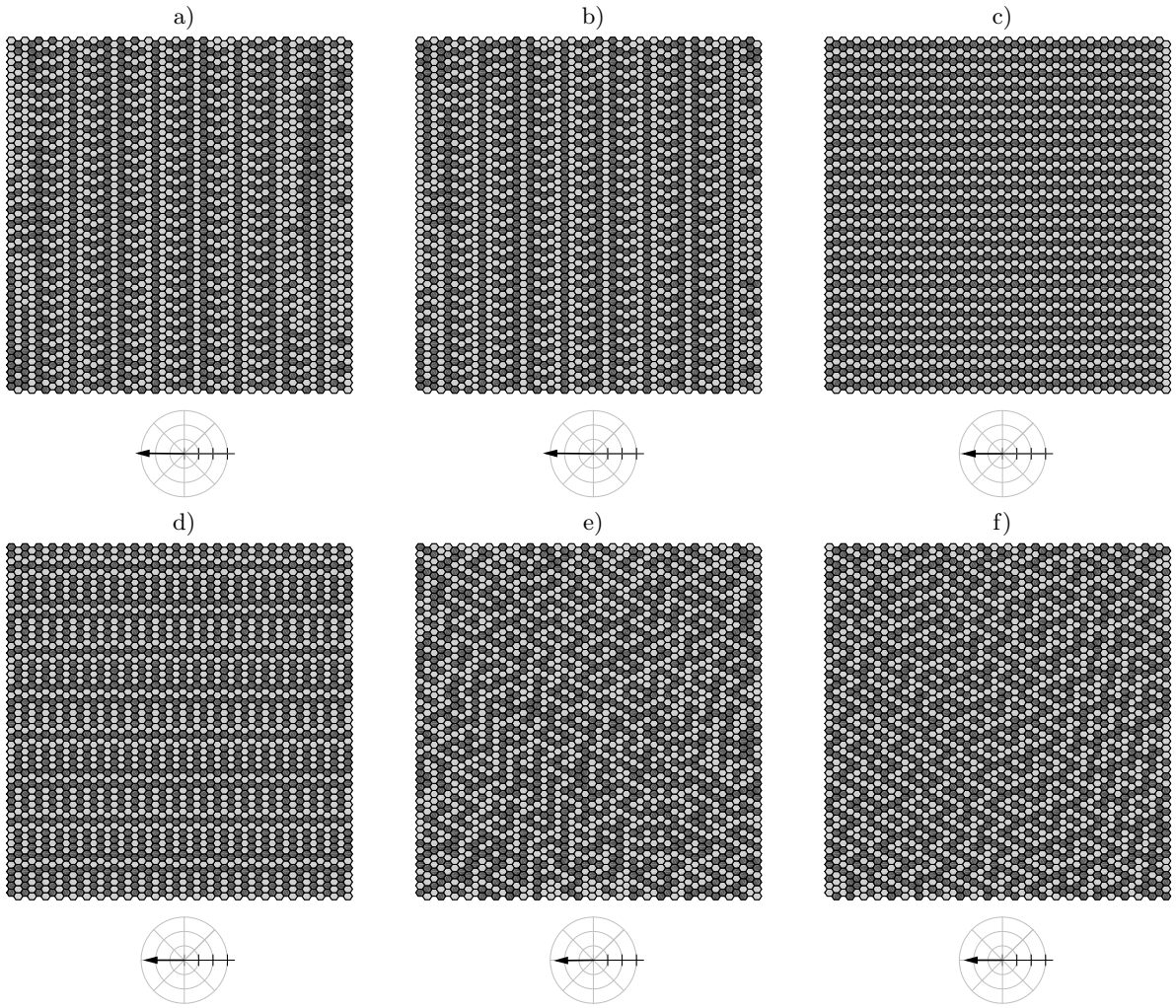

FIG. 22. Examples of attracting states reached by applying four different update schemes to the BHL+L alignment. From top left to bottom right: attracting state reached by a) SRAU1, b) SRAU1, c) RAU1, d) SRAU2, e) DAU, f) DAU. For RAU1 and SRAU2 100 different initial states reached the same attracting network state shown in panel c) and d), respectively. Whereas, applying SRAU1 and DAU lead to a diversity of attracting network structures, which in contrast to the perfect regular structures generated by RAU1 and SRAU2, show "defects". The crosshairs visualize the mucus transport direction and its magnitude of the corresponding attractors (the radial tick interval is set to 0.2 [cells/it.]), i.e. $\vec{v_{g,\infty}}$.

sisting of 5×5 cells arranged in a square lattice assuming open boundaries. The middle panel in Fig.25 illustrates the network topology considering the possible pathways of the mucus droplets. The right panel illustrates the network topology considering the possible locked configurations. Arrows entering a node indicate which nodes may block its oscillation. Arrows leaving a node indicate for which nodes its state and mucus load is relevant to block the nodes the arrows are pointing at. The in-degree of a node is the sum of incoming arrows and correspondingly, the out-degree is the sum of outgoing arrows. The grayscale in the graphs indicate the value of the in- and out-degrees and therewith the prevalent hierarchy among the nodes. If we set open boundaries, marginal nodes in our networks are hardly influenced by their adjacent nodes. It is especially important that nodes at the left and right boundary have no in-degree considering the locked-configurations-rule. Consequently, these nodes won't adapt their oscillatory motions according to their neighbors' motion and act as "leading nodes".
Finally, we observed that some settings need a very regular topology with a prevalent hierarchy among the agents. If this "leadership" of a few nodes is abandoned, which happens when applying toric boundary conditions or importing unciliated cells, hardly any self-organization takes place.

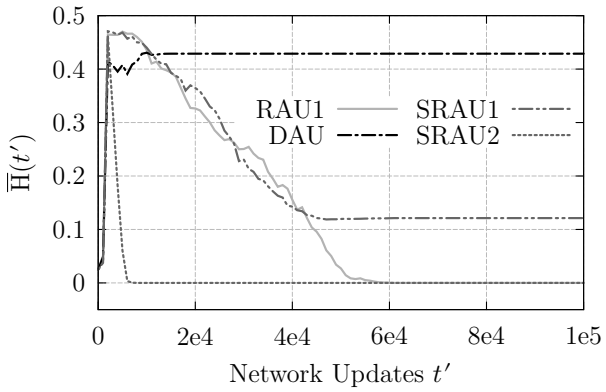

FIG. 23. The curves show the average Hamming distance between the network state of a reference run and four simulation runs for which the initial state has been perturbed with respect to the reference run (1-4% of the nodes have been inverted).

3. Boundary-Driven Structure Emergence Hindered by Unciliated Cells

Unciliated cells can only take up and release mucus droplets and are thus, only passively involved in the state update of adjacent actuators. This means that cells adjacent to unciliated cells obtain a lower in-degree and therefore ascend the hierarchy of actuators. As we randomly distribute unciliated cells, "leading nodes" are no longer only found at the boundaries, but rather are distributed allover the network and consequently, the network topology becomes less regular.

It has been observed that the introduction of unciliated cells hinder the spreading of the structure emergence for those settings for which the structure spreads strictly from an open boundary. Consequently, it seems that some settings require a very regular topology in order to be able to spread allover the network. The panels in Fig.26 show three stages of a simulation for which we introduced 1% of unciliated cells and otherwise applied the same settings as in Fig.24. Unciliated cells are shown in black. It's clearly visible that the structure emergence is hindered by the introduced unciliated cells, as the structure can't spread further than to the first unciliated cells, seen from left. According to this simple observation one could imagine that the influence of the boundaries gets the more restricted the more unciliated cells are incorporated. Further simulations have confirmed this idea.

4. Modular Self-Organization

If we arrange the actuators in the square lattice (USL) and introduce a certain amount of unciliated cells, the array of actuators efficiently evolves to a self-cleaning epithelium. In this case the network topology considering the state update gets strongly changed, what becomes obvious when thinking of the case of sparsely distributed ciliated cells. One can imagine that a group of ciliated cells would be surrounded by unciliated cells forming thereby "ciliated islands" on an otherwise unciliated epithelium. These islands would be hardly interconnected amongst each others when concerning the state updates. How strongly these modules are interconnected depends on the density of ciliated cells. In order to illustrate this modular character introduced by unciliated cells, the topology of the square lattice has been applied together with open boundary conditions and the update DAU for an ensemble with 100 members differing by their initial state. The grid size has been set to 300×300 cells. Fig.27 illustrates the temporal evolution of the corresponding velocity fields. The grayscales illustrate the locally resolved transient time τ_{ij} (in effect the number of network updates it takes for an actuator to reach a local transport speed, which almost amounts to the final area averaged transport speed). The upper panel in Fig.27 corresponds to simulations ran with a dense mat of cells (100% ciliated cells), while in the lower panel 10% of randomly distributed unciliated cells were introduced. The panels represent the ensemble average of the spatially resolved transient times. The darker the color the longer it took until a certain actuator synchronized its movement. The discussed effect of the "leading boundary" is clearly visible in the upper panel of Fig.27, as the gradient in brightness from the left to the right indicates the structure emergence, which sets in at the left boundary and spreads towards the right boundary. On the other hand, as soon as one introduces unciliated cells the self-organization process gets a modular character, as the structure emergence doesn't start at a certain point from which it spreads allover the network, but spreads at several locations simultaneously, which is illustrated by the relatively homogeneous distribution of grayscale in the lower panel in Fig.27. The influence of the boundary is strongly restricted to the marginal nodes at both sides. The larger one chooses the grid size, or the more unciliated cells are introduced, the less important the "dominance" of the marginal actuators gets.

In conclusion, unciliated cells introduce a certain degree of modularity in the network topology as well as in the self-organizing process and therefore, the influence of the choice of boundary conditions can be neglected in the interior of the array, if the array size is chosen large enough and if a realistic amount of unciliated cells is considered.

movie_S5 (see [36]) shows the evolution of the network's state of a simulation run, generated with (100×100, USL, DAU, OP, 20%, 0.5, 10%), exhibiting the typical modular self-organization process leading to modular expression patterns.

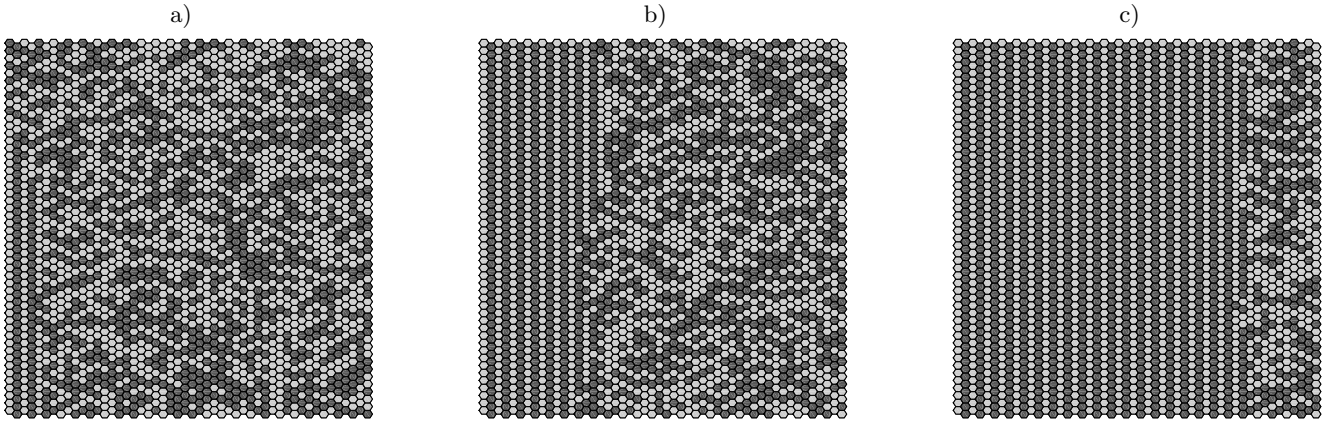

FIG. 24. Three snapshots of the network's state at three different stages of the self-organization process (time increases from panel a-c). The network states were generated by applying RAU1 to the BHL+L alignment with open boundary conditions. The structure emergence sets in at the left boundary and spreads to the right over the whole network.

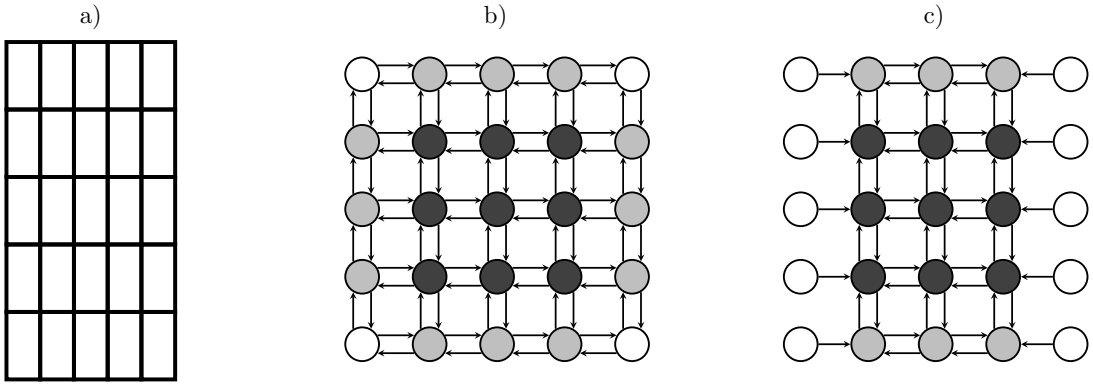

FIG. 25. An array of 5×5 actuators aligned in the square-lattice is shown in panel a). Actuators represent the nodes of the network and local interactions the links. Panel b) shows the network topology considering the exchange of mucus particles among nodes. Panel c) illustrates the network topology considering the state updates. Panel b) and c) correspond to open boundary conditions. In panel c) it can be seen that open boundaries introduce "leading nodes" at the margin.

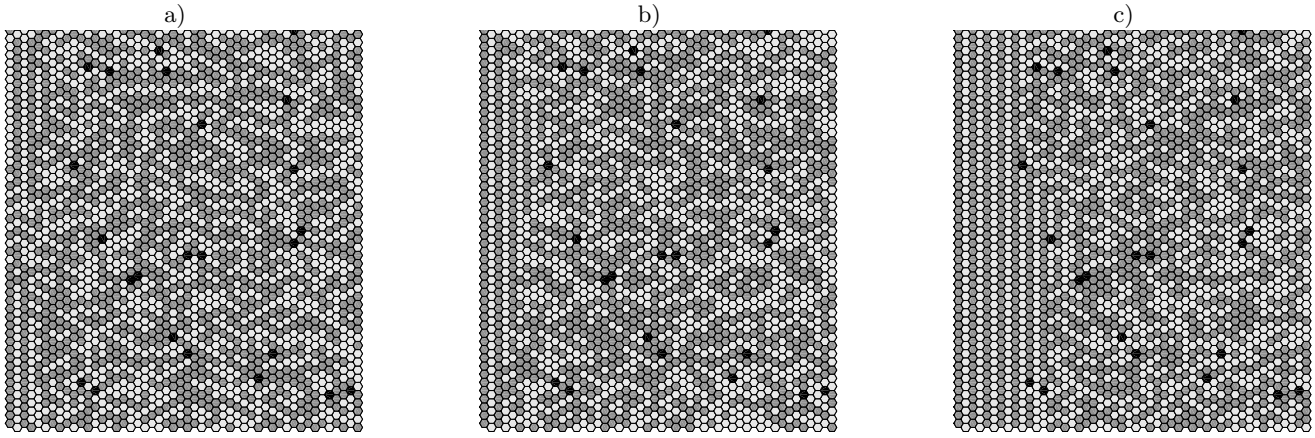

FIG. 26. Three snapshots of the temporal evolution of the model when using the BHL+L alignment (time increases from panel a-c), open boundaries, RAU1 and 1% of randomly distributed unciliated cells. Note that the structure emergence is hindered by unciliated cells.

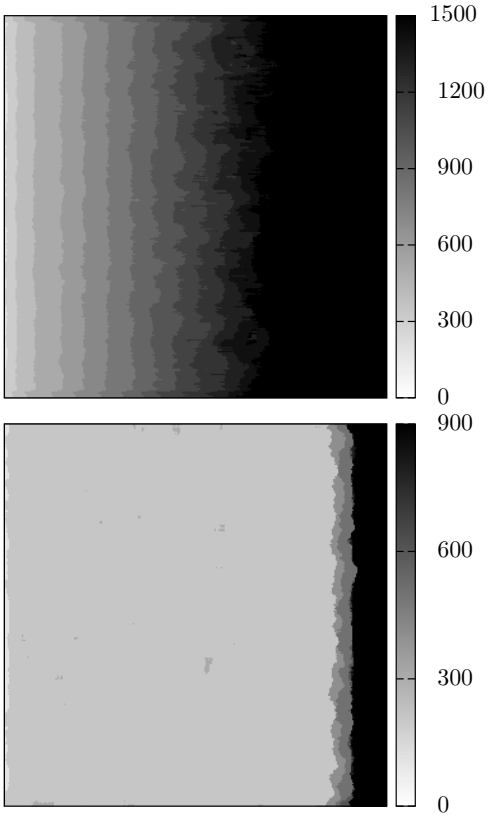

FIG. 27. The grayscale indicates the locally resolved transient time [network updates] (note that there are two different grayscales). Both panels correspond to ensemble averages. The upper panel corresponds to runs having 100% ciliated cells, while the lower panel corresponds to runs with 90% of ciliated cells. The homogeneity in the lower panel indicates that boundary effects may be neglected in the network's interior, if unciliated cells are considered.

5. *Transient Time vs. Network Size*

In this section we point out that unciliated cells may strongly influence the dynamics of ciliated epithelia. As outlined in the previous section unciliated cells import topological modularity. Modularity is an important and promising concept, which is inter alia studied in terms of modular random boolean networks. In [43] it is claimed that topological modularity reduces the probability for damage spreading over the network, what promotes robustness.

In the following we show how unciliated cells affect the dynamics of our network model. As the square lattice is the only cell arrangement leading to a properly self-cleaning state, when introducing unciliated cells, all the results shown in this section refer to the square lattice arrangement.

The transient time has been determined for different array sizes in the range between 50×50 cells^2 and 1000×1000 cells^2 as well as for different fractions of unciliated cells (0%, 2% and 10%). The collected data points are presented in Fig.28. The lines are only guidelines for the eye. Black dots correspond to the dense mat case for which all cells are ciliated. Dark gray diamonds and bright gray stars correspond to 98% and 90% ciliated cells, respectively. One can clearly see that the transient time is not only reduced when introducing unciliated cells, but varies substantially different with increasing array size. While the transient time continuously grows for an array representing a totally ciliated mat with increasing array size, the transient time runs into saturation with increasing array size if unciliated cells are present. As discussed in the former section unciliated cells import not only topological modularity, but also cause the self-organization process to be modular, as the emergence of structure and transport evolves simultaneously in different modules. This finding most probably explains the level off of the transient time with increasing array size if unciliated cells are considered. As the self-organization process takes place in a decentralized manner, it does not depend upon the size of the actuator-array. On the other hand, the transient time continues to increase with increasing array size for an array purely consisting of ciliated cells, which is related to the nature of the structure emergence for these settings. According to the left panel in Fig.24 the self-organization process mainly starts at the left boundary, from where it spreads to the right allover the network. Accordingly, one would expect that the growth of the transient time continues with increasing network size, as it is the case in Fig.28. (The transient time primarily depends on the length of the simulated actuator-array, as the ordered structures expand from the left to the right). As the transient time

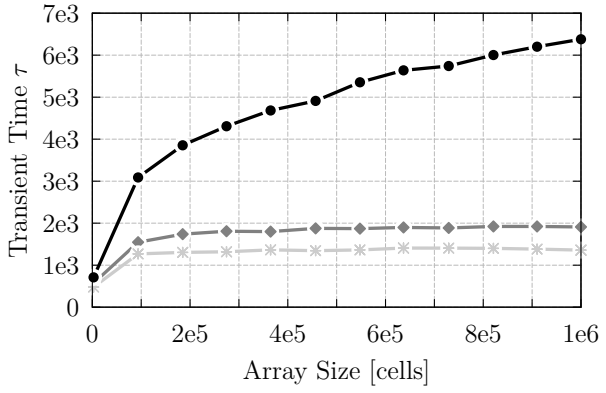

FIG. 28. The graph shows the transient time [iterations] versus network size [cells]. Black dots correspond to a totally dense ciliated mat. Dark gray diamonds and bright gray stars correspond to an array containing 98% and 90% ciliated cells, respectively.

can be seen as a measure for robustness, our results suggest that the imported modularity promotes robustness. Consequently, it seems that the modular topology imports modularity into the self-organization process, which means that the organization of a huge network

gets decomposed into a simultaneous organization of submodules. These submodules can be recognized by examining the spatial structure of the network's state, as it has been observed that the modularity of the expression patterns clearly depend on the density of ciliated cells. The auto-correlation length of attracting network states has been determined for settings differing by the amount of ciliated cells as well as the boundary conditions. As we are interested in the spatial structures of the expression patterns, the grid size has been chosen to 200×200 cells. Fig.29 shows the auto-correlation length [cells] vs. the relative amount of unciliated cells [%] for open and toric boundary conditions. It can be clearly seen that the

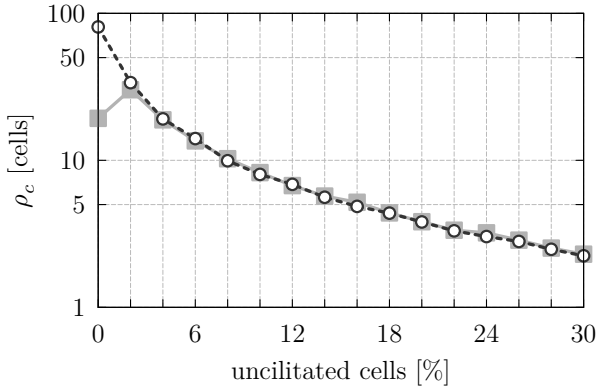

FIG. 29. The graph shows the auto-correlation length [cells] vs. the relative amount of unciliated cells [%] for different boundary conditions. The black circles and bright gray squares correspond to data points derived when using toric and open boundary conditions, respectively.

auto-correlation length, decreases with an increasing portion of unciliated cells. Furthermore, the auto-correlation length is roughly given by the mean distance of unciliated cells. Consequently, unciliated cells may play a further role in the self-organization process on the ciliated airway epithelium, as the appearance of the previously described patch-work character may be strongly influenced by the distribution of unciliated and ciliated cells.

IV. DISCUSSION

The aim of this study is twofold: On the one hand, we want to make the self-organized spatio-temporally coordinated ciliary beat patterns as well as the self-organized fluid transport across multiciliated epithelia plausible. We suggest that the cooperation among ciliated cells emerges from locally interacting oscillating cilia bundles belonging to different ciliated cells. As our goal was to keep our model as simple as possible, we present a virtual self-cleaning epithelium model based on symmetrically interacting two-state actuators, which we formulate in terms of an adaptive boolean network. In the framework of adaptive boolean networks the ciliated cells represent the nodes of the network and discrete mucus droplets establish the local interactions and therefore the network's topology. In Sec.III D we demonstrate the coevolution of the network's state and its topology, which is a characteristic property of adaptivity and represents the self-organized coevolution of ciliary beating patterns and associated fluid transport.

On the other hand, we report our insights to our system's dynamics we gained by conducting parameter studies. In the following we discuss the observed effects of the update scheme, the boundary conditions and the amount of unciliated cells on the dynamics of our network model and how these effects may relate to real mucociliary systems.

As we formulate our epithelium model in terms of a discretized asynchronous multi-agent network, the question of how to update the network arises. The introduced update schemes are meant to represent different possible intercellular signaling mechanisms (membrane potentials and calcium waves). Only settings using either the deterministic asynchronous update (DAU) or the alignment BHL+L, or both, guide the network towards properly self-cleaning states (Table I). Settings using BHL+L or DAU introduce a local recurrent temporal coupling among adjacent actuators inducing an asymmetry of the local interactions. Fig.18 suggests that the prevalent asymmetry, such as the initial speed associated with a specific parameter setting, increases the probability for efficient self-organization towards self-cleaning states. In any case none of the roughly 11'000 simulations exhibiting an initial transport speed of less than 0.01 cells/it self-organizes efficiently towards a properly self-cleaning state.

Furthermore, the application of the deterministic update scheme (DAU) seems to generate less well ordered attracting network states. This behavior is exemplary illustrated in Fig.22 showing a perfectly ordered attracting state for the random asynchronous update (RAU1), slightly less well ordered network states for the semi-random update schemes (SRAU1 and SRAU2) and finally, the least ordered attracting states for the deterministic update scheme (DAU). All settings using the deterministic update scheme have consistently generated patterns showing "defects" perpendicular to the direction of the update scheme and maximum correlation along the direction of the update. Fig.16 represents an autocorrelogram of an extreme case: maximum correlation is found into the direction of the primary update direction (from right to left), which is most probably caused by the local temporal coupling among actuators, while there seems to be almost no local temporal coupling from the top to the bottom, what leads to typically elongated autocorrelograms if DAU is applied.

Finally, the less strict organization the network generates when using DAU may lead to more flexible dynamics as in the case of a perturbation the system does not simply recover its original attracting state, but conforms to the changes by running into a completely different attractor

(see Fig.23).

The effects of different update schemes on the dynamics of multi-agent systems are still being investigated. In [30] six different update schemes have been applied on one-dimensional cyclic cellular automata to compare the resulting dynamics. It has been concluded that deterministic update schemes confer a degree of flexibility upon the system dynamics, what compares well to the observed conforming character of our model settings using a deterministic update scheme. Consequently, so far, the findings show evidence that in various asynchronous processes leading to self-organization, a deterministic update scheme leads to more realistic dynamics (flexibility and robustness) and may therefore be favored by evolution [28]. Recall, however, that "deterministic" does not mean that actuators would displace the mucus in a pre-determined direction. Rather, the transport direction evolves through the interplay between the update asymmetry and the largely stochastic interactions.

Finally, we would like to point out the possible effect of unciliated cells on the dynamics on ciliated epithelia. The topology of our network model is primarily given by the formulation of the local interaction rules, the choice of the boundary conditions and the amount of unciliated cells. As we have outlined in Sec.III F 4 the amount of unciliated cells introduces a certain degree of topological modularity. The topological modularity in turn causes a modular self-organization, which means that the self-organization does not start at a specific point or boundary on the grid - as it has been observed for completely dense mats of ciliated cells - but starts in each module simultaneously. This modular character of the self-organization leads to the size-independence of the transient time, reported in Sec.III F 5. Consequently, modularity may provide robustness even to networks as large as the human ciliated airway epithelium consisting of more than 10^9 cells [44], as perturbations quickly fade away. Furthermore, the modular topology leads to modular expression patterns, the size of which are roughly given by the mean distance of unciliated cells (as shown in Fig.29). Finally, the finding of a modular self-organization caused by the underlying modular topology providing a highly robust patch-work amongst actuators, provides a consistent explanation of the modular expression patterns previously reported in experimental studies aimed at the quantitative description of the modulation wave fields on the tracheal epithelium [7].

We conclude that an intercellular signaling mechanism is probable on ciliated epithelia, as deterministic update schemes drive the model towards robust self-organized states, which can still conform to changes. We suggest that the patchy expression patterns of the modulation wave field observed on real ciliated epithelia may be the result of the underlying modular topology, which is primarily formed by the distribution of ciliated and unciliated cells. This patch-work character among ciliated cells may be highly robust due to a modular self-organization, which prevents perturbations to spread over the whole network. Furthermore, the boundary conditions may become irrelevant on epithelia being either large enough or having a low amount of ciliated cells.

We close this study by hypothesizing that the modular organization of the dynamics on ciliated epithelia may be seen as a robust size-independent construction plan of nature, which leads to properly self-cleaning airways in organisms being as small as new born mice as well as in adult giraffes.

[1] R. W. Linck, in *Encyclopedia of Life Sciences* (John Wiley & Sons, Ltd, Chichester, UK, 2009).
[2] P. Satir and S. T. Christensen, Annual review of physiology **69**, 377 (2007).
[3] H. Sui and K. H. Downing, Nature **442**, 475 (2006).
[4] S. a. Burgess, M. L. Walker, H. Sakakibara, P. J. Knight, and K. Oiwa, Nature **421**, 715 (2003).
[5] M. J. R. et al. Oliveira, Lung **181**, 275 (2003).
[6] C. G. Plopper, a. T. Mariassy, D. W. Wilson, J. L. Alley, S. J. Nishio, and P. Nettesheim, Experimental lung research **5**, 281 (1983).
[7] M. Ryser, a. Burn, T. Wessel, M. Frenz, and J. Rička, European Biophysics Journal **37**, 35 (2007).
[8] S. M. Ross and S. Corrsin, Journal of Applied Physiology **37**, 333 (1974).
[9] D. J. Smith, E. a. Gaffney, and J. R. Blake, Bulletin of Mathematical Biology **69**, 289 (2007).
[10] D. J. Smith, E. a. Gaffney, and J. R. Blake, Bulletin of Mathematical Biology **69**, 1477 (2007).
[11] W. Lee, P. Jayathilake, Z. Tan, D. Le, H. Lee, and B. Khoo, Computers & Fluids **49**, 214 (2011).
[12] W. F. Marshall, Nature cell biology **12**, 314 (2010).
[13] I. H. Riedel-Kruse, A. Hilfinger, J. Howard, and F. Jülicher, HFSP Journal **1**, 192 (2007).
[14] A. Hilfinger and F. Jülicher, Physical Biology **5**, 016003 (2008).
[15] A. Hilfinger, A. K. Chattopadhyay, and F. Jülicher, Physical Review E - Statistical, Nonlinear, and Soft Matter Physics **79**, 1 (2009), arXiv:0906.0547.
[16] J. Elgeti and G. Gompper, Proceedings of the National Academy of Sciences of the United States of America **110**, 4470 (2013).
[17] S. M. Mitran, Computers and Structures **85**, 763 (2007).
[18] S. Gueron, K. Levit-Gurevich, N. Liron, and J. J. Blum, Proceedings of the National Academy of Sciences of the United States of America **94**, 6001 (1997).
[19] M. Salathe, Annual review of physiology **69**, 401 (2007).
[20] J. Rutland and R. U. De Iongh, The New England Journal of Medicine **323**, 1681 (1993).
[21] R. De Iongh and J. Rutland, Journal of clinical pathology **42**, 613 (1989).
[22] M. E. P. Rautiainen, European Respiratory Journal **1**, 257 (1988).
[23] C. H. Lee, S. S. Lee, J.-h. Mo, I.-s. Kim, S.-h. Quan,

S. Y. Wang, W.-j. Yi, C.-s. Rhee, and Y.-g. Min, Acta Oto-Laryngologica **125**, 571 (2005).
[24] W.-J. Yi, K.-S. Park, C.-H. Lee, C.-S. Rhee, and S.-W. Nam, IEEE Transactions on Bio-medical Engineering **49**, 269 (2002).
[25] L. B. Wong, I. F. Miller, and D. B. Yeates, Journal of Applied Physiology **75**, 458 (1993).
[26] A. Van As and I. Webster, Environmental Research **7**, 1 (1974).
[27] M. Geiser, V. Im Hof, W. Siegenthaler, R. Grunder, and P. Gehr, Microscopy Research and Technique **36**, 428 (1997).
[28] C. Gershenson, in *Artificial Life IX, Proceedings of the Ninth International Conference on the Simulation and Synthesis of Living Systems*, edited by J. Pollack, M. Bedau, P. Husbands, T. Ikegami, and R. Watson (MIT Press, 2004) pp. 238–243, arXiv:0402006v3 [arXiv:nlin].
[29] C. Gershenson, in *Artificial Live VIII: Proceedings of the Eight International Conference on Artificial Life*, edited by R. K. Standish, M. A. Bedau, and H. A. Abbass. (MIT Press, 2002) pp. 1–8.
[30] D. Cornforth, D. G. Green, and D. Newth, Physica D: Nonlinear Phenomena **204**, 70 (2005).
[31] J. Ricka, Physik in unserer Zeit **41**, 74 (2010).
[32] E. M. Purcell, American Journal of Physics **45**, 3 (1977).
[33] M. Aldana, S. Coppersmith, and L. P. Kadanoff, in *Perspectives and Problems in Nolinear Science* (Springer New York, 2003) pp. 23–89.
[34] T. Gross and B. Blasius, Journal of the Royal Society, Interface **5**, 259 (2008), arXiv:0709.1858.
[35] R. Hanel, S. Thurner, and M. Gell-Mann, Proceedings of the National Academy of Sciences **111**, 6905 (2014), arXiv:arXiv:1404.5650v1.
[36] *Supplemental material at [URL]*.
[37] F. Greil, *Dynamics of Boolean networks*, Ph.D. thesis, T.U. Darmstadt (2009), arXiv:1307.0757.
[38] A. Wuensche, Complexity International **6** (1998).
[39] C. Gershenson, in *Workshop and Tutorial Proceedings, Ninth International Conference on the Simulation and Synthesis of Living Systems (ALife IX)*, edited by M. Bedau, P. Husbands, T. Hutton, S. Kumar, and H. Suzuki (2004) pp. 160–173.
[40] F. Greil, Frontiers in Plant Science **3** (2012), 10.3389/fpls.2012.00178.
[41] T. Niedermayer, B. Eckhardt, and P. Lenz, Chaos **18** (2008), 10.1063/1.2956984.
[42] T. Rohlf and S. Bornholdt, in *Adaptive Networks* (Springer Berlin Heidelberg, 2009) pp. 73–106, arXiv:0811.0980v1.
[43] R. Poblanno-Balp and C. Gershenson, Artificial Life **17**, 331 (2011), arXiv:arXiv:1101.1893v2.
[44] R. R. Mercer, M. L. Russell, V. L. Roggli, and J. D. Crapo, American journal of respiratory cell and molecular biology **10**, 613 (1994).